

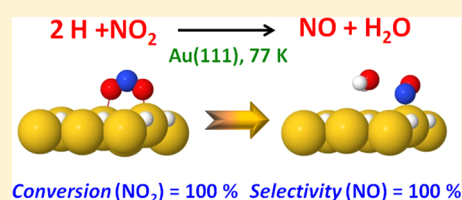
# Highly Selective, Facile NO<sub>2</sub> Reduction to NO at Cryogenic Temperatures on Hydrogen Precovered Gold

Ming Pan,<sup>†</sup> Hyung Chul Ham,<sup>†,§</sup> Wen-Yueh Yu,<sup>†</sup> Gyeong S. Hwang,<sup>†</sup> and C. Buddie Mullins<sup>\*,†,‡</sup>

<sup>†</sup>Department of Chemical Engineering and <sup>‡</sup>Department of Chemistry and Biochemistry, Center for Nano and Molecular Science and Technology, Texas Materials Institute, and Center for Electrochemistry, University of Texas at Austin, Austin, Texas 78712-0231, United States

**S** Supporting Information

**ABSTRACT:** We have discovered that NO<sub>2</sub> is reduced to NO at 77 K by hydrogen precovered gold in vacuum. Here, we investigate the partial reduction of NO<sub>2</sub> to NO on an atomic-hydrogen populated model gold catalyst for a more fundamental understanding of the surface chemistry of hydrogenation. Gold-based catalysts have been found to be active for many hydrogenation reactions, but few related fundamental studies have been conducted. Our experimental results reveal a high catalytic activity for gold: indeed, NO<sub>2</sub> is reduced to NO with 100% conversion and 100% selectivity at temperatures lower than 120 K. Density functional theory calculations and reflection–absorption infrared spectroscopy measurements indicate that HNO<sub>2</sub> and N<sub>2</sub>O<sub>3</sub> are intermediates which are highly dependent on surface hydrogen concentrations; subsequent hydrogenation of HNO<sub>2</sub> and dissociation of N<sub>2</sub>O<sub>3</sub> upon annealing induces the production of NO and H<sub>2</sub>O.



## 1. INTRODUCTION

Gold-based catalysts have been studied for a wide range of energy-efficient processes<sup>1–12</sup> as well as for hydrogenation chemistry.<sup>13–21</sup> NO<sub>x</sub> reduction is also a potential application for gold catalysts and has been briefly investigated with H<sub>2</sub>,<sup>22,23</sup> propene,<sup>24</sup> or CO<sup>25,26</sup> as reducing agents, but the mechanisms are not well understood. Here, we report a mechanistic study of NO<sub>2</sub> reduction to NO by atomic hydrogen using a model gold catalyst. The experimental results indicate that NO<sub>2</sub> can be converted to NO on H/Au(111) at a cryogenic temperature, 77 K. Unexpectedly high NO<sub>2</sub> conversion (100%) and NO selectivity (100%) are observed at temperatures lower than 120 K suggesting a highly selective and facile NO<sub>2</sub> reduction process mediated by the gold surface. Our previous work shows that atomic H has a small desorption activation energy of ~0.29 eV on Au(111),<sup>27,28</sup> so these weakly chemisorbed hydrogen adatoms likely play a key role in facilitating such unique hydrogenation chemistry. Density functional theory (DFT) calculations and reflection–absorption infrared spectroscopy (RAIRS) measurements provide insights into the relevant reaction mechanisms in which surface-bound HNO<sub>2</sub> and N<sub>2</sub>O<sub>3</sub> are intermediates.

In this work, we employ a Au(111) single crystal as the model catalyst which can be considered as a planar representative of supported gold nanoparticles. In addition, since molecular hydrogen has a high energetic barrier to dissociation on model gold surfaces,<sup>29,30</sup> we employ gas-phase H atoms to populate the surface so that hydrogenation chemistry can be studied. We hope that our study will assist in identifying the role of gold on classical supported catalysts where H<sub>2</sub> dissociates on the periphery sites and likely spills over onto the gold particles.<sup>31</sup> Although this work only yields NO<sub>2</sub>

reduction to NO, high conversion of NO<sub>2</sub> and high selectivity to NO have been observed, indicating unique surface chemistry for gold and providing insights into its catalytic activity in hydrogenation reactions.

## 2. EXPERIMENTAL SECTION

**2.1. Experimental Apparatus and Sample Cleaning.** All experiments were conducted in a supersonic molecular beam apparatus under ultrahigh-vacuum (UHV) conditions with a base pressure of  $2 \times 10^{-10}$  Torr.<sup>32–35</sup> The differentially pumped chamber consists of a source chamber to generate molecular beams and a scattering chamber for analysis, which contains a quadrupole mass spectrometer (QMS), an Auger electron spectrometer (AES), and low-energy electron diffraction (LEED) optics. A circular gold sample is installed on a pair of copper power leads which can be cooled to 77 K by a liquid nitrogen reservoir and resistively heated to 900 K by a proportional–integral–derivative (PID) controller. A K-type thermocouple was applied to measure sample temperatures. Prior to every experiment, the sample was cleaned by exposing to an intense NO<sub>2</sub> molecular beam with the surface held at 800 K for 2 min.<sup>36,37</sup> Periodically, contamination on the sample was removed by Ar<sup>+</sup> ion bombardment. The sample cleanliness and surface structure were verified by AES and LEED. Infrared (IR) measurements were carried out in another UHV chamber which has a Fourier transform infrared spectrometer and a mercury–cadmium–telluride (MCT) detector.<sup>38</sup>

**2.2. Reactant Dosing.** We employed a home-built device to generate H atoms via an electron-beam-heated high-temperature tungsten capillary in which molecular hydrogen is converted to H atoms or vibrationally excited molecules which dissociate on Au(111) at 77 K.<sup>39,40</sup> The relative coverage of hydrogen and deuterium atoms is determined by comparing to the saturated surface. In order to avoid NO<sub>2</sub> decomposition and purity degradation, the gas handling system,

Received: October 3, 2012

Published: December 11, 2012

including valves and tubes, was passivated by exposing to a relatively high pressure of NO<sub>2</sub> for a prolonged time. NO<sub>2</sub> was delivered onto the Au(111) surface via a molecular beam initiating from a device with an array of nozzles, each with the same aperture size and separate plumbing to ensure reagent purity as delivered to the sample. The coverage of NO<sub>2</sub> is determined based on temperature programmed desorption (TPD) spectra from Au(111), where 1 monolayer (ML) nitrogen dioxide is considered as the amount yielding a maximum integrated area under the monolayer desorption feature. Water was introduced onto the sample surface in a molecular beam with a flux rate of 0.067 ML/sec.<sup>35,41</sup>

**2.3. DFT Calculations.** The calculations reported herein were performed on the basis of spin polarized DFT within the generalized gradient approximation (GGA-PW91),<sup>42</sup> as implemented in the Vienna ab-initio simulation package (VASP).<sup>43</sup> The projector augmented wave (PAW) method with a planewave basis set was employed to describe the interaction between core and valence electrons.<sup>44</sup> An energy cutoff of 350 eV was applied for the planewave expansion of the electronic eigenfunctions. For the Brillouin zone integration, we used a (4 × 4 × 1) Monkhorst–Pack mesh of *k* points to calculate geometries and total energies. Reaction pathways and barriers were determined using the nudged elastic band method (NEBM) with eight intermediate images for each elementary step.<sup>45</sup> For Au model surfaces, we constructed a four atomic-layer slab with a hexagonal 3 × 3 unit cell. The slab is separated from its periodic images in the vertical direction by a vacuum space corresponding to seven atomic layers. The lattice constant for bulk Au is predicted to be 4.18 Å, close to the experimental value of 4.08 Å. While the bottom two layers of the four-layer slab were fixed at corresponding bulk positions, the upper two layers were fully relaxed using the conjugate gradient method until residual forces on all the constituent atoms became smaller than 5 × 10<sup>-2</sup> eV/Å.

### 3. RESULTS AND DISCUSSION

**3.1. NO Evolution From H/Au(111) via NO<sub>2</sub> Reduction at 77 K.** We first performed molecular beam reactive scattering (MBRS) experiments to investigate the reduction of NO<sub>2</sub> on gold. A molecular beam-blocking shutter can be rapidly moved out/in of the path of the beam allowing/stopping the impingement of NO<sub>2</sub> molecules (the beam flux rate is 0.1 ML/sec with a kinetic energy of ~0.1 eV) on the Au(111) surface. A quadrupole mass spectrometer (QMS) was used to identify gas-phase species reacting/scattering from the sample. Figure 1 displays QMS signals from species evolving from the sample during the 20 s of NO<sub>2</sub> (2.0 ML) impingement onto both clean and H (θ<sub>H,rel</sub> = 1) preadsorbed Au(111) at a surface temperature of 77 K. Figure 1a illustrates a control experiment: Here NO<sub>2</sub> was impinged onto the clean Au(111) surface [without precovering the gold with H atoms] at *t* = 0 s where NO<sub>2</sub> molecules both adsorb and scatter off the sample and cause the QMS intensity increase observed. As the NO<sub>2</sub> beam strikes the surface over the entire 20 s experiment, a constant intensity for scattered NO<sub>2</sub> is observed, suggesting that scattering/adsorption of NO<sub>2</sub> dominates this process (with no hint of reaction).

With the Au(111) surface covered by H atoms at unity relative coverage (determined by comparing to a H-saturated sample surface), the MBRS experiments were performed with results shown in Figure 1b, indicating the evolution of NO from the surface at 77 K. Note that the sticking probability of NO<sub>2</sub> is ~60% on H-covered Au(111). In the initial ~4–5 s of impingement by the NO<sub>2</sub> beam, the NO signal shows virtually identical behavior to the experiment on clean Au(111) as shown in Figure 1a, suggesting an induction period. From *t* = 5 to 15 s, the signal for NO shows a significant evolution lasting for approximately 10 s and reaching a peak value at *t* = 10 s,

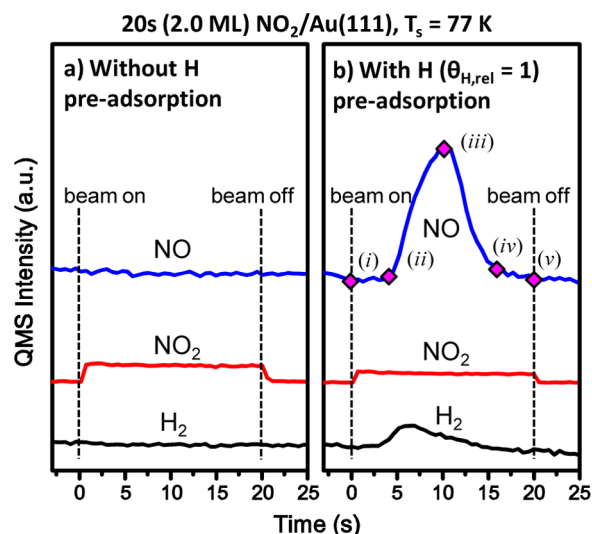


**Figure 1.** MBRS of NO<sub>2</sub>. The beam strikes onto (a) the clean Au(111) surface (b) the H (relative coverage θ<sub>H,rel</sub> = 1) atom precovered Au(111) surface at 77 K. The NO<sub>2</sub> beam was impinged on the surface from 0 to 20 s. The points denoted (i–v) mark specific times corresponding to measurements discussed later in the paper. The NO<sub>2</sub> beam flux is 0.1 ML/sec. Note that (a,b) have the same Y-axis scale.

demonstrating a reaction between adsorbed NO<sub>2</sub> and H adatoms. The points labeled from (i–v) indicate various experimental stages including (i) beam on, (ii) beginning, (iii) peak, (iv) end of NO evolution, and (v) beam off, respectively, which are discussed later with regard to relevant TPD measurements, DFT calculations, and RAIRS studies. In contrast to NO, the NO<sub>2</sub> signal behaves similarly as in the control experiment, with a constant intensity. We also observe that the MBRS experiment results in H<sub>2</sub> evolution at 77 K. This phenomenon is also likely related to NO<sub>2</sub> reduction, which activates H atoms and induces the desorption of H<sub>2</sub> at low temperature.

Note that both gaseous NO<sub>2</sub> and NO give signals for mass 30 in our mass spectrometer. For NO<sub>2</sub>, the signal for mass 30 arises from the gas-phase dissociation (into NO and O) of the molecule in the electron bombardment ionization process, whereas for NO mass 30 is the parent mass. Thus, the MBRS spectra for NO in Figure 1 have been modified by subtracting the mass 30 component due to NO<sub>2</sub> from the signals at mass 30 in order to provide a better description of the NO evolution during NO<sub>2</sub> impingement on H/Au(111). The unaltered data are shown in Figure S1.

**3.2. TPD Measurements Regarding the Different Reaction stages.** To further explore the mechanistic details of this reaction, we conducted TPD measurements as a function of NO<sub>2</sub> coverage on the H-precovered (θ<sub>H,rel</sub> = 1) Au(111) surface at 77 K. The various NO<sub>2</sub> coverages are correlated to impingement times of the NO<sub>2</sub> beam and various stages of the reaction [i.e., points (i–v) displayed in Figure 1b]. Figure 2a,b displays TPD spectra for masses 30, 46, and 18, respectively, corresponding to NO + NO<sub>2</sub>, NO<sub>2</sub>, and H<sub>2</sub>O, evolving from Au(111) upon heating the sample surface from 77 to 300 K at a ramp rate of 1 K/s. The black curves are acquired from a control experiment with unity relative H coverage on Au(111) but zero coverage of NO<sub>2</sub> (corresponding to point (i) in Figure 1b), in which, as expected, no desorption products for masses 30, 46, or 18 are observed.

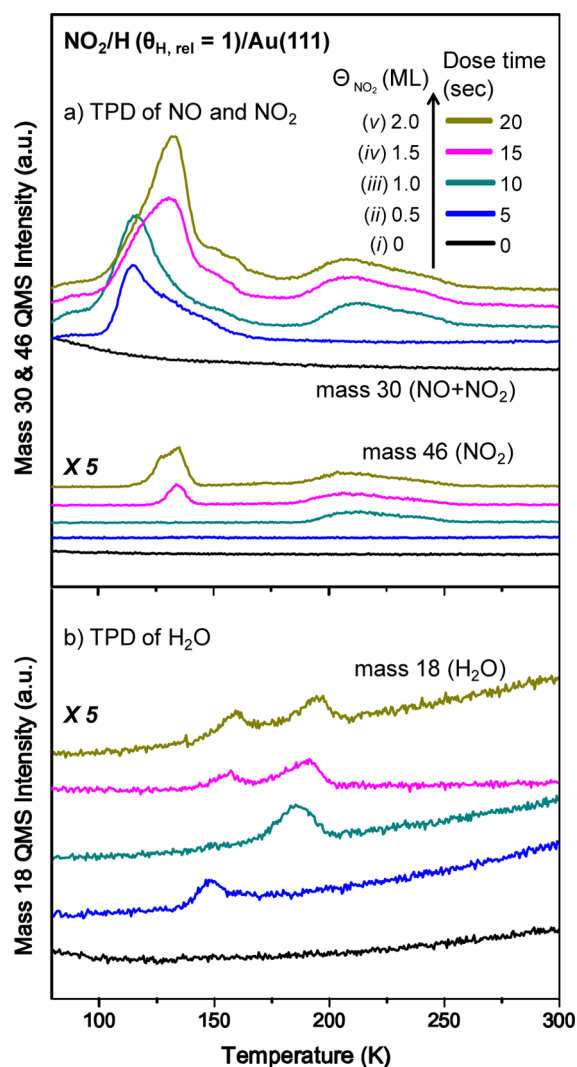


**Figure 2.** TPD studies from  $\text{NO}_2$  and H coadsorbed Au(111). TPD spectra of mass 30, 46, and 18 after various coverages of  $\text{NO}_2$  impingement to Au(111) with preadsorption of hydrogen atoms (relative coverage  $\theta_{\text{H,rel}} = 1$ ) at 77 K. Note that (a) and (b) have the same scale for the Y-axis.

Next we studied the H/Au(111) surface ( $\theta_{\text{H,rel}} = 1$ ) coadsorbed with 0.5 ML of  $\text{NO}_2$  [this is equivalent to 5 s of  $\text{NO}_2$  impingement and reaches the point at which the evolution of NO begins; i.e., point (ii) in Figure 1]. There is no desorption feature observed from the TPD spectrum for mass 46 indicating that the adsorbed  $\text{NO}_2$  has completely reacted with the H adatoms yielding a 100% conversion. The TPD spectrum for mass 30 in Figure 2a shows a desorption feature with a peak at  $\sim 120$  K, which can be completely attributed to desorbing NO rather than a mass fragment of  $\text{NO}_2$  (since no mass 46 desorbs). During the measurement, no other reduced products, such as  $\text{N}_2\text{O}$ ,  $\text{N}_2$ , or  $\text{NH}_3$  were detected indicative of a high selectivity (100%) toward NO.

TPD measurements from the H-precovered ( $\theta_{\text{H,rel}} = 1$ ) Au(111) surface after 10 s of  $\text{NO}_2$  impingement were performed as shown in Figure 2a. This exposure of  $\text{NO}_2$  results in a coverage of 1.0 ML and produces the maximum in NO evolution in MBRS [point (iii) in Figure 1b]. In the TPD measurements shown in Figure 2, the sample was heated to 300 K inducing a single broad feature from  $\sim 190$ –260 K in

the spectrum for mass 46 indicative of  $\text{NO}_2$  monolayer desorption, which is also apparent in mass 30 as the ionized fragment of  $\text{NO}_2$ . However, a significant desorption feature for mass 30 also appears with a peak at  $\sim 120$  K. This feature is not duplicated in mass 46 and clearly suggests  $\text{NO}_2$  reduction on the surface with subsequent NO desorption.

Point (iv) in Figure 1 indicates that the evolution of NO nearly vanishes after 15 s of  $\text{NO}_2$  impingement (1.5 ML) on the H precovered Au(111) surface. On a comparably covered surface, the TPD experiment produces two desorption features with similar shape for both mass 30 and 46 (Figure 2a), in which peak temperatures are consistent with the distinct desorption features of  $\text{NO}_2$  from clean Au(111).<sup>46</sup> Thus, we infer that the mass 30 signal is primarily (but not exclusively) from  $\text{NO}_2$  fragmentation with little parent NO. Note that with decreasing H surface concentration [no detection of  $\text{H}_2$  desorption at point (iv) indicating that H atoms are completely consumed] and a constant  $\text{NO}_2$  beam flux, a portion of the  $\text{NO}_2$  molecules directly adsorb on Au(111) without reacting and also contribute to the desorption features we measure in Figure 2a. We estimate that the evolved NO after point (iv), as shown in Figure 1b, is from  $\sim 6.1\%$  of the total  $\text{NO}_2$  molecules that have adsorbed on the surface during 15 s of  $\text{NO}_2$  beam impingement. Further extending the  $\text{NO}_2$  impingement time until 20 s [point (v) in Figure 1b] results in a larger desorption feature for  $\text{NO}_2$  in mass 30 and 46 at  $\sim 130$  K as shown in Figure 2a, when the surface reactions are ending, and  $\text{NO}_2$  is beginning to populate the multilayer on Au(111).

Figure 2b displays TPD spectra for water produced from the surface reaction between H adatoms and adsorbed  $\text{NO}_2$  molecules on Au(111). The black curve illustrates a control experiment indicating, as expected, no water formation on the solely H-covered surface. With increasing  $\text{NO}_2$  coverage on the H-precovered surface, water desorption sequentially yields for point (ii) a single peak at  $\sim 150$  K [consistent with the characteristic desorption peak of water on clean Au(111)],<sup>47</sup> for (iii) a single peak at  $\sim 190$  K and for (iv) and (v) two features apparent at both  $\sim 160$  and  $\sim 190$  K. This water desorption behavior is likely related to the progress of reaction involving H adatoms and  $\text{NO}_2$  as well as their concentrations on the surface and will be discussed more later.

**3.3. DFT Calculations to Explore Mechanisms for NO Evolution.** The results of our DFT calculations are summarized in Table 1 for which two types of surfaces have been compared regarding the H adatom coverage on Au(111) (here a low hydrogen coverage,  $\theta_{\text{H}}$ , corresponds to more empty sites, represented by  $\theta_{\text{E}}$ ). Figure 3 shows a representative

**Table 1. Energetics/Barriers of Surface Reactions During MBRS Experiments**

reaction	$\theta_{\text{H}} \sim 1$ ( $\theta_{\text{E}} \sim 0$ )		$\theta_{\text{H}} \sim 0$ ( $\theta_{\text{E}} \sim 1$ )	
	$\Delta E$ (eV)	$E_{\text{a}}$ (eV)	$\Delta E$ (eV)	$E_{\text{a}}$ (eV)
(i–ii) Induction				
$\text{NO}_2(\text{g}) \rightarrow \text{NO}_2$	–0.30		–0.81	
$\text{NO}_2 + \text{H} \rightarrow \text{H}_{\text{dw}}\text{ONO}$	–1.13	0.04	–0.45	0.55
$\text{H}_{\text{dw}}\text{ONO} \rightarrow \text{H}_{\text{up}}\text{ONO}$	–0.02	0.28	–0.24	0.35
(ii–iv) NO Evolution				
$\text{H} + \text{H}_{\text{up}}\text{ONO} \rightarrow \text{NO} + \text{H}_2\text{O}$	–0.72	0.47	–0.90	0.30
$\text{NO} + \text{NO}_2 \rightarrow \text{N}_2\text{O}_3$			–0.03	0.27
(iv–v) Postevolution				
$\text{NO}_2(\text{g}) \rightarrow \text{NO}_2$			–0.81	



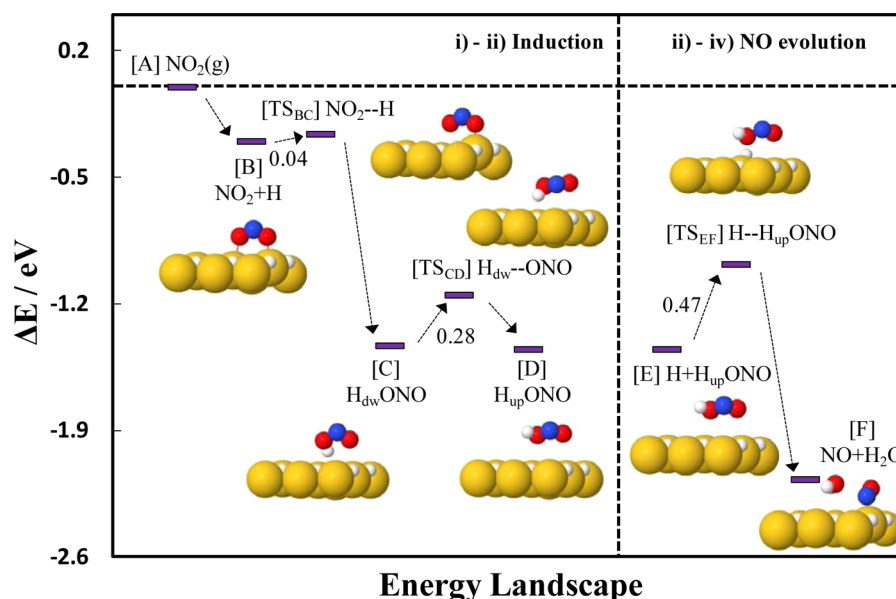


**Figure 3.** Predicted potential energy diagram for NO evolution from the NO<sub>2</sub> and H coadsorbed Au(111) surface. This diagram indicates the intermediate and transition-state configurations on Au(111) with high precovered H at  $\theta_{\text{H}} = 1$ . Note that the configurations of surface species are not affected by H coverages. The big yellow and the small blue, red, and white balls indicate Au, N, O, and H atoms, respectively.

energy diagram for NO<sub>2</sub> reduction and NO evolution on Au(111) at  $\theta_{\text{H}} = 1$ , illustrating species adsorption and transition states. It should be noted that the geometric configurations of molecules and intermediates on the surface are independent of surface H concentrations (i.e., the schematic configurations in Figure 3 are the same for low H coverage).

We first investigate the initial NO<sub>2</sub> activation on H covered Au(111) by calculating the adsorption energy of NO<sub>2</sub> and the reaction energetic/barrier for NO<sub>2</sub> + H → HNO<sub>2</sub>. As shown in Figure 3 and Table 1, we find that on the H saturated surface ( $\theta_{\text{H}} \sim 1$  or  $\theta_{\text{E}} \sim 0$ ), NO<sub>2</sub> exothermically adsorbs [ $E_{\text{ad}} = 0.30$  eV] at the top-bridge-top site with the two O moieties of NO<sub>2</sub> bonded to Au atoms on H covered Au(111). In the next step, we see that adsorbed NO<sub>2</sub> can readily react with neighboring H adatoms with a very low barrier (0.04 eV), producing a *cis* form of HNO<sub>2</sub> (indicated by H<sub>dw</sub>ONO where H points toward the surface). Here, the rotational barrier of the H atom in H<sub>dw</sub>ONO for forming a *trans* HNO<sub>2</sub> (H<sub>up</sub>ONO where H points away from the surface) is predicted to be 0.28 eV. Together with the exothermic NO<sub>2</sub> adsorption energy, this result suggests that NO<sub>2</sub> can be trapped in the form of H<sub>dw</sub>ONO or H<sub>up</sub>ONO on H-covered Au(111) at 77 K.

This process dominates the early period in the MBRS measurement from 0–5 s and represents the initial induction period [the period (i–ii)] before the evolution of NO, as shown in Figure 1b. The computational results display the relatively high barriers for the reaction of HNO<sub>2</sub> with neighboring H atoms during the induction period (H + H<sub>up</sub>ONO → NO + H<sub>2</sub>O,  $E_{\text{a}} = 0.47$  eV). Note that we only focus on the H<sub>up</sub>ONO state because the reaction between H<sub>dw</sub>ONO and H always occurs via the H<sub>up</sub>ONO state), implying that NO cannot evolve at 77 K. Our TPD results show desorption peaks for NO and H<sub>2</sub>O at  $\sim 120$  and  $\sim 150$  K, respectively, as displayed in Figure 2a,b. We also compared other possible reaction mechanisms for NO production, such as NO<sub>2</sub> → NO + O ( $E_{\text{a}} = 1.98$  eV) and H<sub>up</sub>ONO → NO + OH ( $E_{\text{a}} = 0.81$  eV), both of which have a higher energetic barrier and cannot be considered viable mechanisms. Due to the high barrier for

HONO dissociation and the ease of NO<sub>2</sub> trapping by H adatoms (which is exothermic by 1.13 eV), we think that the single-step Eley–Rideal (ER) reaction of NO<sub>2</sub>(g) + H → OH + NO(g) is highly unlikely. In addition, the induction period we observe also indicates that the reduction of NO<sub>2</sub> to NO is not following an ER mechanism. Otherwise, NO would evolve immediately after the NO<sub>2</sub> beam strikes the H/Au(111) surface (at  $t = 0$  s).

With further exposure of NO<sub>2</sub> to the surface by the beam, NO begins to evolve from the surface. This production of NO at 77 K is related to the reduction of the barrier for the reaction H + H<sub>up</sub>ONO → NO + H<sub>2</sub>O due to the increase of available empty surface sites near H<sub>up</sub>ONO (called “near empty sites” in later discussion) through H<sub>2</sub> desorption which has been observed during MBRS as shown in Figure 1b. Our previous study indicated that H atoms weakly chemisorb on Au(111) and H<sub>2</sub> recombinative desorption has a small activation energy of  $\sim 0.29$  eV.<sup>27,48</sup> In contrast, the adsorption of NO<sub>2</sub> on H/Au(111) and HNO<sub>2</sub> formation is an exothermic process and releases heat (0.30 and 1.13 eV, respectively as shown in Table 1), which likely activates a fraction of the H adatoms leading to recombinative H<sub>2</sub> desorption at 77 K.

According to our DFT calculations, the barrier for H + H<sub>up</sub>ONO → NO + H<sub>2</sub>O strongly depends on the number of near empty surface sites around HNO<sub>2</sub>. A larger number of near empty surface sites leads to a lower reaction barrier. In Table 1, we display the barriers for the surface reaction H + H<sub>up</sub>ONO → NO + H<sub>2</sub>O for different coverages of neighboring empty surface sites around HNO<sub>2</sub>. We find that the barrier ( $E_{\text{a}} = 0.30$  eV) at  $\theta_{\text{E}} \sim 1$  is substantially lower than the  $\theta_{\text{E}} \sim 0$  case ( $E_{\text{a}} = 0.47$  eV), implying that the large availability of near empty surface sites around HNO<sub>2</sub> plays an important role in enhancing NO evolution through the H + H<sub>up</sub>ONO reaction at 77 K. Therefore, it can be concluded that the induction period prior to NO evolution at 77 K is partly due to the time needed for generation of near empty sites. Figure S2a shows that lower initial H coverages cause a longer induction period and smaller production of NO during MBRS, indicating that the formation

of  $\text{HNO}_2$  is a rate-determining step which is promoted by high coverage of H adatoms as shown in Table 1. These results suggest that NO evolution is not only affected by reaction kinetics but also influenced thermodynamically. The use of deuterium lengthens the induction period and significantly reduces the production of NO by a factor of 10, as shown in Figure S2b. These experimental results could be due to quantum tunneling of H/D and a primary kinetic isotope effect.

Additionally, a portion of the nascent NO directly evolves from the surface at 77 K, whereas the other part reacts with adsorbed  $\text{NO}_2$  on the Au(111) surface via the reaction  $\text{NO} + \text{NO}_2 \rightarrow \text{N}_2\text{O}_3$  where dinitrogen trioxide is generated as the second intermediate (DFT calculations show a barrier of 0.27 eV for  $\text{NO} + \text{NO}_2 \rightarrow \text{N}_2\text{O}_3$ ). Annealing the sample surface causes the thermal dissociation of intermediate  $\text{N}_2\text{O}_3$  producing NO and  $\text{NO}_2$  as shown in Figure 2a(iii). TPD measurements indicate that H adatoms are depleted at the end of NO evolution ( $t \sim 15$  s). During the period from point (iii) to (v) in Figure 1b, a large fraction of  $\text{NO}_2$  molecules adsorb intact on the surface with low reaction probability due to the lack of H adatom coverage.

DFT calculations indicate that water is produced from the reactions  $\text{H} + \text{NO}_2 \rightarrow \text{HNO}_2$  and  $\text{H} + \text{HNO}_2 \rightarrow \text{NO} + \text{H}_2\text{O}$ . Thus, the production of water is correlated to the concentration of surface hydrogen atoms. In addition, Koel has reported that  $\text{NO}_2$  has a strong interaction with water on Au(111) and can stabilize water resulting in desorption at a higher temperature.<sup>49</sup> Figure S3 indicates that water can be stabilized by  $\text{NO}_2$  on the surface yielding a desorption peak temperature at  $\sim 190$  K. This is in agreement with the TPD spectra for water in Figure 2b: (1) at  $t = 5$  s  $\text{NO}_2$  is fully converted to NO via an  $\text{HNO}_2$  intermediate and thus is unavailable to interact with the adsorbed water, so there is a single water desorption feature at  $\sim 150$  K; (2) at  $t = 10$  s  $\text{NO}_2$  is produced via  $\text{N}_2\text{O}_3$  decomposition and interacts with water, shifting the desorption feature to the higher temperature of  $\sim 190$  K; (3) with further  $\text{NO}_2$  impingement, and the surface reaction progressing (to  $t = 15$  and 20 s) more water is generated on the surface and induces a desorption feature again at 160 K. In addition, Figure S4 shows TPD experiments with fixed  $\text{NO}_2$  coverage but varying H coverages on Au(111). Figure S4b shows that water has a single desorption feature at  $\sim 190$  K for low H coverages and induces the other desorption feature at  $\sim 160$  K with increasing H coverages (i.e., more water is formed). This series of experiments clearly indicates that water desorption is  $\text{NO}_2$  concentration dependent on coadsorbed H/Au(111), consistent with the above discussion.

**3.4. Infrared Studies to Investigate Reaction Intermediates.** To enhance microscopic understanding of  $\text{NO}_2$  reduction, vibrational spectroscopy was employed to study the Au(111) surface coadsorbed with H adatoms and  $\text{NO}_2$  at 77 K. Figure 4a shows vibrational spectra for  $\text{NO}_2$  on clean Au(111) with varying coverages as a control experiment, and the infrared spectra are in excellent agreement with previously published results by Wang and Koel.<sup>49,50</sup> The distinct absorption peaks for fundamental vibrational modes of  $\text{NO}_2$  are evident at 1182 and 808  $\text{cm}^{-1}$  which correspond to  $\nu(\text{NO}_2)$  (symmetric and asymmetric stretching vibrations) and  $\delta_s(\text{NO}_2)$  (symmetric bending mode) normal modes, respectively. At  $\theta = 1.0$  ML, the dimer of  $\text{NO}_2$  is formed with the features for  $\text{N}_2\text{O}_4$  at 1759, 1298, and 784  $\text{cm}^{-1}$  which are attributed to the  $\nu_s(\text{NO}_2)$ ,  $\nu_a(\text{NO}_2)$ , and  $\delta_s(\text{NO}_2)$  modes, respectively. In addition, peaks are apparent at 1907 and 1256  $\text{cm}^{-1}$  indicating features for

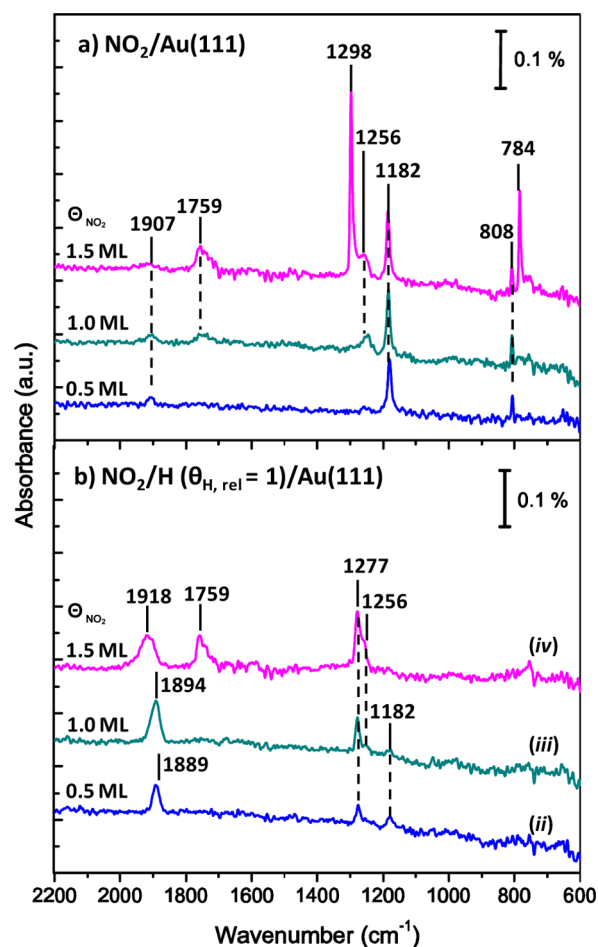


**Figure 4.** RAIRS spectra of  $\text{NO}_2$ . RAIRS measurements were conducted on (a) clean Au(111) and (b)  $\theta_{\text{H,rel}} = 1$  of H precovered Au(111). In MRBS experiments,  $\text{NO}_2$  was impinged onto H/Au(111) at 77 K reaching the end of the induction period (the beginning of NO evolution) at point (ii), the peak of NO evolution at point (iii), and the end of NO evolution at point (iv) as illustrated in Figure 1b. Note that (a) and (b) have the same scale for the Y-axis.

$\text{N}_2\text{O}_3$  with the  $\nu(\text{NO})$  and  $\nu_a(\text{NO}_2)$  modes, which are reported by Wang and Koel from the reaction between background NO and surface  $\text{NO}_2$ .<sup>50</sup>

After adsorbing  $\text{NO}_2$  on the H precovered surface and achieving a variety of reaction stages [(ii–iv)], we acquired RAIRS spectra at 77 K revealing significant differences in comparison to the control experiments on the clean surface. Figure 4b shows most of the characteristic features for  $\text{NO}_2$ ,  $\text{N}_2\text{O}_4$ , and  $\text{N}_2\text{O}_3$  on H/Au(111), however the intensities are noticeably diminished compared to Figure 4a, indicating a decrease in the  $\text{NO}_2$  concentration due to the reaction with H adatoms. However, with H coadsorbed on the surface, we observe a new feature located in the range of 1850–2000  $\text{cm}^{-1}$ , which could result from reaction intermediates,  $\text{HNO}_2$  and  $\text{N}_2\text{O}_3$ . We propose this band be assigned to the  $\nu(\text{NO})$  mode in  $\text{HNO}_2$  or in  $\text{N}_2\text{O}_3$ , respectively. The transformation from  $\text{HNO}_2$  to  $\text{N}_2\text{O}_3$  with  $\text{NO}_2$  coverage increasing on the surface blue-shifts the new feature from 1889 to 1918  $\text{cm}^{-1}$ . Additionally, we examined the IR spectra after heating the surface to various temperatures regarding those three stages as shown in Figure S5. The feature at 1889  $\text{cm}^{-1}$  decreases upon heating the surface to 125 K. In contrast, the 1918  $\text{cm}^{-1}$  feature is more stable and remains constant until annealing the sample

to 150 K. This observation confirms that those two features are responsible for the different surface species,  $\text{HNO}_2$  and  $\text{N}_2\text{O}_3$ . We also note that a feature at  $1182\text{ cm}^{-1}$  appears when heating the surface to above 150 K, indicating the formation of  $\text{NO}_2$  which likely stems from the decomposition of  $\text{N}_2\text{O}_3$ . The surface infrared spectroscopy measurements at various reaction stages show consistency with MBRS, TPD, and DFT results, clarifying the formation of two intermediates ( $\text{HNO}_2$  and  $\text{N}_2\text{O}_3$ ).

#### 4. CONCLUSIONS

In summary, we have observed  $\text{NO}_2$  reduction to  $\text{NO}$  on the H atom precovered Au(111) surface at 77 K. During MBRS measurements, adsorbing  $\text{NO}_2$  on H/Au(111) causes  $\text{NO}$  to evolve from the surface at 77 K after a brief induction period. The reaction during the induction period yields a high  $\text{NO}_2$  conversion (100%) and remarkable selectivity (100%) toward  $\text{NO}$  (for low  $\text{NO}_2$  coverages with annealing to 120 K) revealing unique catalytic properties for gold in hydrogenation reactions. TPD investigations also provide detailed information demonstrating the production of  $\text{NO}$  and water upon heating the surface. A mechanism is proposed concerning  $\text{HNO}_2$  and  $\text{N}_2\text{O}_3$  as intermediates which are identified by infrared spectroscopy and DFT calculations. Further, this study shows that weakly bound hydrogen plays a key role in hydrogenation chemistry on gold surfaces and provides some fundamental understanding of the high activity of gold-based catalysts for selective hydrogenation processes.

#### ■ ASSOCIATED CONTENT

##### Supporting Information

Original data for  $\text{NO}_2$  reduction at 77 K; MBRS experimental results for  $\text{NO}_2$  reduction with varying H (and D) coverages and subsequent TPD measurements; interaction of water with  $\text{NO}_2$  on Au(111); IR spectra acquired from Au(111) with coadsorption of  $\text{NO}_2$  and H upon annealing the sample to various temperatures. This material is available free of charge via the Internet at <http://pubs.acs.org>.

#### ■ AUTHOR INFORMATION

##### Corresponding Author

mullins@che.utexas.edu

##### Present Address

<sup>§</sup>Fuel Cell Research Center, Korea Institute of Science and Technology (KIST), Seoul, 136–791, Republic of Korea

##### Notes

The authors declare no competing financial interest.

#### ■ ACKNOWLEDGMENTS

We acknowledge the generous support of the Department of Energy (DE-FG02-04ER15587) and the Welch Foundation (F-1436 for C.B.M. and F-1535 for G.S.H.). Ming Pan acknowledges the William S. Livingston Fellowship for financial support.

#### ■ REFERENCES

- (1) Haruta, M.; Kobayashi, T.; Sano, H.; Yamada, N. *Chem. Lett.* **1987**, 405–408.
- (2) Gong, J. L.; Mullins, C. B. *J. Am. Chem. Soc.* **2008**, *130*, 16458–16459.
- (3) Cumaratanunge, L.; Delgass, W. N. *J. Catal.* **2005**, *232*, 38–42.

- (4) Kim, T. S.; Stiehl, J. D.; Reeves, C. T.; Meyer, R. J.; Mullins, C. B. *J. Am. Chem. Soc.* **2003**, *125*, 2018–2019.
- (5) Fu, Q.; Saltsburg, H.; Flytzani-Stephanopoulos, M. *Science* **2003**, *301*, 935–938.
- (6) Gong, J. L.; Mullins, C. B. *Acc. Chem. Res.* **2009**, *42*, 1063–1073.
- (7) Min, B. K.; Friend, C. M. *Chem. Rev.* **2007**, *107*, 2709–2724.
- (8) Xu, B.; Liu, X.; Haubrich, J.; Friend, C. M. *Nature Chem.* **2010**, *2*, 61–65.
- (9) Epling, W. S.; Hoflund, G. B.; Weaver, J. F.; Tsubota, S.; Haruta, M. *J. Phys. Chem.* **1996**, *100*, 9929–9934.
- (10) Kim, J.; Dohnalek, Z.; Kay, B. D. *J. Am. Chem. Soc.* **2005**, *127*, 14592–14593.
- (11) Schumacher, N.; Boisen, A.; Dahl, S.; Gokhale, A. A.; Kandoi, S.; Grabow, L. C.; Dumesic, J. A.; Mavrikakis, M.; Chorkendorff, I. *J. Catal.* **2005**, *229*, 265–275.
- (12) Rodriguez, J. A.; Ma, S.; Liu, P.; Hrbek, J.; Evans, J.; Perez, M. *Science* **2007**, *318*, 1757–1760.
- (13) Sakurai, H.; Tsubota, S.; Haruta, M. *Appl. Catal., A* **1993**, *102*, 125–136.
- (14) Hugon, A.; Delannoy, L.; Louis, C. *Gold Bull.* **2008**, *41*, 127–138.
- (15) Galvagno, S.; Schwank, J.; Parravano, G. *J. Catal.* **1980**, *61*, 223–231.
- (16) Cardenas-Lizana, F.; Gomez-Quero, S.; Idriss, H.; Keane, M. A. *J. Catal.* **2009**, *268*, 223–234.
- (17) Gluhoi, A. C.; Bakker, J. W.; Nieuwenhuys, B. E. *Catal. Today* **2011**, *154*, 13–20.
- (18) Mohr, C.; Hofmeister, H.; Radnik, J.; Claus, P. *J. Am. Chem. Soc.* **2003**, *125*, 1905–1911.
- (19) Choudhary, T. V.; Sivadinarayana, C.; Datye, A. K.; Kumar, D.; Goodman, D. W. *Catal. Lett.* **2003**, *86*, 1–8.
- (20) Jia, J. F.; Haraki, K.; Kondo, J. N.; Domen, K.; Tamaru, K. *J. Phys. Chem. B* **2000**, *104*, 11153–11156.
- (21) Corma, A.; Serna, P. *Science* **2006**, *313*, 332–334.
- (22) Galvagno, S.; Parravano, G. *J. Catal.* **1978**, *55*, 178–190.
- (23) Salama, T. M.; Ohnishi, R.; Shido, T.; Ichikawa, M. *J. Catal.* **1996**, *162*, 169–178.
- (24) Nguyen, L. Q.; Salim, C.; Hinode, H. *Appl. Catal., B* **2010**, *96*, 299–306.
- (25) Ilieva, L.; Pantaleo, G.; Sobczak, J. W.; Ivanov, I.; Venezia, A. M.; Andreeva, D. *Appl. Catal., B* **2007**, *76*, 107–114.
- (26) Kantcheva, M.; Samarskaya, O.; Ilieva, L.; Pantaleo, G.; Venezia, A. M.; Andreeva, D. *Appl. Catal., B* **2009**, *88*, 113–126.
- (27) Pan, M.; Pozun, Z. D.; Yu, W.-Y.; Henkelman, G.; Mullins, C. B. *J. Phys. Chem. Lett.* **2012**, *3*, 1894–1899.
- (28) Pan, M.; Pozun, Z. D.; Brush, A. J.; Henkelman, G.; Mullins, C. B. *ChemCatChem* **2012**, *4*, 1241–1244.
- (29) Sault, A. G.; Madix, R. J.; Campbell, C. T. *Surf. Sci.* **1986**, *169*, 347–356.
- (30) Hammer, B.; Norskov, J. K. *Nature* **1995**, *376*, 238–240.
- (31) Fujitani, T.; Nakamura, I.; Akita, T.; Okumura, M.; Haruta, M. *Angew. Chem., Int. Ed.* **2009**, *48*, 9515–9518.
- (32) Davis, J. E.; Karseboom, S. G.; Nolan, P. D.; Mullins, C. B. *J. Chem. Phys.* **1996**, *105*, 8362–8375.
- (33) Davis, J. E.; Nolan, P. D.; Karseboom, S. G.; Mullins, C. B. *J. Chem. Phys.* **1997**, *107*, 943–952.
- (34) Pan, M.; Hoang, S.; Gong, J.; Mullins, C. B. *Chem. Commun.* **2009**, 7300–7302.
- (35) Pan, M.; Hoang, S.; Mullins, C. B. *Catal. Today* **2011**, *160*, 198–203.
- (36) Bartram, M. E.; Koel, B. E. *Surf. Sci.* **1989**, *213*, 137–156.
- (37) Saliba, N.; Parker, D. H.; Koel, B. E. *Surf. Sci.* **1998**, *410*, 270–282.
- (38) Flaherty, D. W.; Berglund, S. P.; Mullins, C. B. *J. Catal.* **2010**, *269*, 33–43.
- (39) Bischler, U.; Bertel, E. *J. Vac. Sci. Technol., A* **1993**, *11*, 458–460.
- (40) Bornscheuer, K. H.; Lucas, S. R.; Choyke, W. J.; Partlow, W. D.; Yates, J. T. *J. Vac. Sci. Technol., A* **1993**, *11*, 2822–2826.

- (41) Hoang, S.; Pan, M.; Mullins, C. B. *J. Phys. Chem. C* **2009**, *113*, 21745–21754.
- (42) Perdew, J. P.; Wang, Y. *Phys. Rev. B* **1992**, *45*, 13244–13249.
- (43) Kresse, G.; Furthmüller, J. *VASP the guide*; Vienna University of Technology: Vienna, Austria, 2001.
- (44) Blochl, P. E. *Phys. Rev. B* **1994**, *50*, 17953–17979.
- (45) Henkelman, G.; Uberuaga, B. P.; Jonsson, H. *J. Chem. Phys.* **2000**, *113*, 9901–9904.
- (46) McClure, S. M.; Kim, T. S.; Stiehl, J. D.; Tanaka, P. L.; Mullins, C. B. *J. Phys. Chem. B* **2004**, *108*, 17952–17958.
- (47) Ojifinni, R. A.; Froemming, N. S.; Gong, J.; Pan, M.; Kim, T. S.; White, J. M.; Henkelman, G.; Mullins, C. B. *J. Am. Chem. Soc.* **2008**, *130*, 6801–6812.
- (48) Pan, M.; Flaherty, D. W.; Mullins, C. B. *J. Phys. Chem. Lett.* **2011**, 1363–1367.
- (49) Wang, J.; Koel, B. E. *Surf. Sci.* **1999**, *436*, 15–28.
- (50) Wang, J.; Koel, B. E. *J. Phys. Chem. A* **1998**, *102*, 8573–8579.